CHEMISTRY OF MATERIALS

Fe Cations Control the Plasmon Evolution in $CuFeS_2$ Nanocrystals

Yuan Yao,[†] Anuj Bhargava,[†] and Richard D. Robinson*

Cite This: *Chem. Mater.* 2021, 33, 608−615

ABSTRACT: Plasmonic semiconductor nanocrystals have become an appealing avenue for researching nanoscale plasmonic effects due to their wide spectral range (visible to infrared) and great tunability compared to traditional precious metal nanocrystals. $CuFeS_2$ is an exciting semiconductor that has a prominent plasmon absorption band in the visible range (~498 nm). Previous work has reported conflicting accounts of the existence of the plasmon band and the cation oxidation states in this material. In this work, we answer these outstanding questions and determine the origin of the plasmonic behavior in $CuFeS_2$ by characterizing the nucleation and growth stages of the reaction through a series of *ex situ* and *in situ* probes (e.g., X-ray absorption spectroscopy and X-ray emission spectroscopy). We show that the plasmon formation is driven by the band structure modification from Fe^{2+} incorporation into the nanocrystals. As opposed to the pure Cu^{1+}/Fe^{3+} predicted by DFT studies, a mixed oxidation state of Cu^{1+}/Cu^{2+} and Fe^{2+}/Fe^{3+} is observed, indicating that the chalcopyrite phase ($CuFeS_2$) encompasses a range of oxidation states depending on the synthesis conditions. From our combined results, we propose a reaction mechanism for the $CuFeS_2$ synthesis and outline a method to verify the phase purity of the material. Overall, this study provides a theoretical basis for tuning plasmon intensity by changing the cation oxidation state through various routes such as synthesis time and temperature.

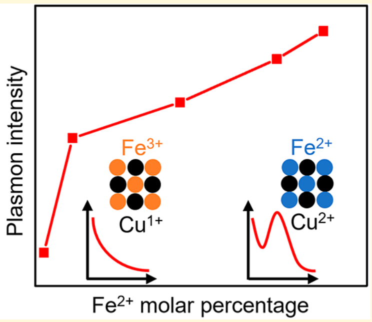

■ INTRODUCTION

The study of localized surface plasmon resonances (LSPRs) is a celebrated and mature field for noble metal nanocrystals (NCs), but they are the focus of frontier research in semiconductor nanocrystals. Unlike metals, semiconductors have a controllable charge carrier density (10^{18}−10^{22} cm^{-3}), enabling tunability of the LSPR through a wide spectral range (from near-visible to infrared).[1−4] LSPRs have been widely investigated in a variety of semiconductors including oxides[5−7] and sulfides[3,8] as well as in a host of more exotic ternary systems.[9,10] In the family of ternary systems, the recently rediscovered $CuFeS_2$ has been increasingly explored due to its plasmon absorption in the visible range (~500 nm) as well for its ability for chemical tunability and its ease of synthesis.[9,11,12]

Despite the initial focus as an iron ore,[13] comprehensive studies about $CuFeS_2$'s magnetic properties, electric properties, and optical properties were not published until the late 1950s to early 1960s.[14−19] Multiple absorption bands (1.0 eV, 2.1 eV) were found in the optical spectrum, which was explained by the existence of an intermediate band.[19] Recently, nanometer-sized $CuFeS_2$ has gained attention due to its interesting properties such as small band gap,[20] visible range plasmon absorption,[11] promising Seebeck coefficient,[21] as well as potential applications as a battery cathode material[22] and photothermal agent.[23]

Despite the substantial research done on this material, several controversies about $CuFeS_2$ are unresolved. One of the heavily debated questions is the existence and the origin of the plasmon peak. Despite having nearly identical X-ray diffraction patterns corresponding to the chalcopyrite phase, an ~500 nm absorption band is observed in some samples,[11,20,23,2425] but absent in others.[12,16,26] For example, Pandey *et al.*[12] synthesized $CuFeS_2$ nanocrystals using a heat-up method, and no plasmon was observed in the absorption spectrum. However, their follow-up study[20] using a modified synthesis method produced nearly identically sized $CuFeS_2$ particles with a strong plasmon at 2.5 eV. Another major question concerning $CuFeS_2$ nanomaterials is the oxidation state of the cations in $CuFeS_2$. Some studies found mixed oxidation states (Fe^{2+}, Fe^{3+}, Cu^{2+}, Cu^{1+}) present with varying relative concentrations for both Cu and Fe.[27,28] For example, Todd *et al.*[27] used X-ray absorption near-edge structure (XANES) to confirm the existence of both Fe^{2+}/Fe^{3+} and Cu^{1+}/Cu^{2+}, whereas other works,[29−31] including recent DFT calculations,[23] have found that the Fe and Cu cations are only present as a single species (i.e., Fe^{3+} and Cu^{1+}). For example, Sawatzky *et al.*[30] identified the cation oxidation states as Fe^{3+} and Cu^{1+} using the Mossbauer effect and X-ray photoelectron spectroscopies (XPS). As we report in our work here, these two major questions—the existence of the plasmon peak and the

Received: September 27, 2020
Revised: December 14, 2020
Published: January 5, 2021

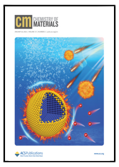

https://dx.doi.org/10.1021/acs.chemmater.0c03829

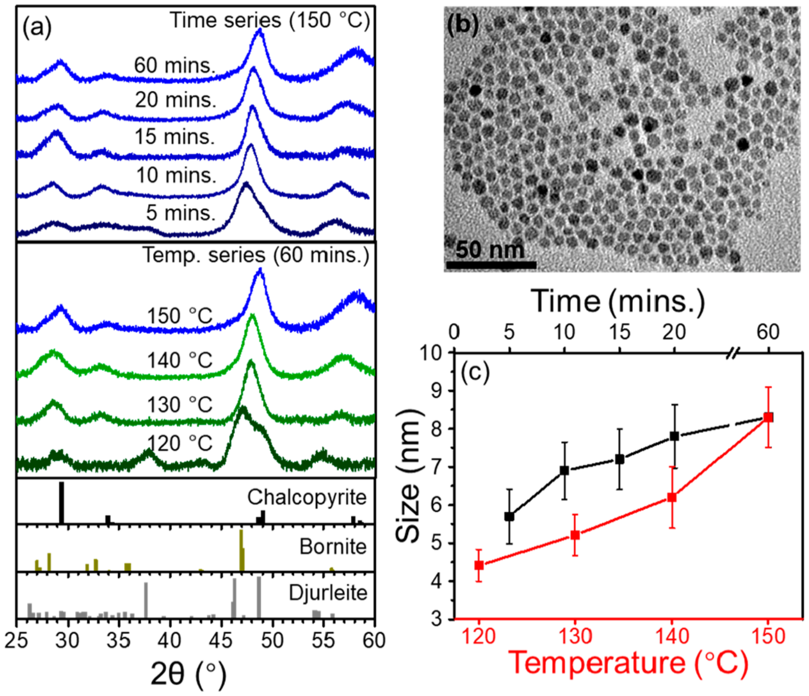

Figure 1. Structural and size evolution of $CuFeS_2$ nanocrystals synthesized at different reaction times and temperatures. (a) X-ray diffraction patterns for nanocrystals grown for (top) different lengths of time at 150 °C and (bottom) 60 min at temperatures 120, 130, 140, and 150 °C. At early times (i.e., 5 min−150 °C) or low temperatures (i.e., 60 min−120 °C), the patterns correspond to a mixed phase between chalcopyrite ($CuFeS_2$), djurleite ($Cu_{1.94}S$), and bornite (Cu_5FeS_4) phases. With increasing time/temperature, the samples transition to pure chalcopyrite phase. (b) Representative transmission electron microscopy (TEM) image of the nanocrystals (140 °C−60 min sample). (c) Size and relative size dispersion for all nanocrystals determined using TEM images. For time series nanocrystals, size increases from 5.7 to 8.3 nm with size dispersion ∼ 11% for all samples. For temperature series samples, size increases from 4.4 to 8.3 nm with size dispersion ∼ 10%.

oxidation state of the cations—are inextricably linked and can explain disparities in past literatures.

We resolve the above issues by studying the synthesis products of $CuFeS_2$ through *ex situ* and *in situ* K-edge X-ray absorption spectroscopy (XAS) and *ex situ* X-ray emission spectroscopy (XES), coupled with UV−vis absorption spectroscopy and X-ray diffraction (XRD). These experiments enable us to systematically track the evolution of cation species and their concentrations during nanocrystal growth and correlate this evolution to the plasmonic behavior in $CuFeS_2$. We find that a mixed cation oxidation state of Cu^{1+}/Cu^{2+} and Fe^{2+}/Fe^{3+} is present in $CuFeS_2$ samples that exhibit the chalcopyrite phase in X-ray diffraction. The Cu^{1+}/Cu^{2+} and Fe^{2+}/Fe^{3+} relative concentrations vary based on synthesis conditions (reaction temperature and reaction time), and the stability of multiple mixed oxidation states indicates that the chalcopyrite structure does not have a fixed cation oxidation state. More importantly, we show that the formation of the plasmon is determined by the band structure modification induced by Fe^{2+} incorporation.

■ EXPERIMENTAL SECTION

The heat-up method is adopted for synthesizing the $CuFeS_2$ nanocrystals. Metal precursor is prepared by dissolving 40.5 mg (0.25 mmol), 33.5 mg (0.25 mmol), and 200 mg of $FeCl_3$, $CuCl_2$, and ascorbic acid in 1:1 oleylamine (OLA) and 1-octadecene (ODE) solution. 75 mg (0.5 mmol) of penicillamine is dissolved in 2.5 mL of ODE and 2.5 mL of OLA solution to make the sulfur precursor. Both solutions are degassed and purged with nitrogen before mixing at 50 °C. The solution is heated up to the target reaction temperatures (120, 130, 140, and 150 °C) and held at that temperature for different lengths of times (5, 10, 15, 20, and 60 min). After completion of the reaction, nanocrystals are collected by dissolving in a 1:1 hexane/acetone mixture and centrifuged for at least 3 times before being stored in a desiccator. Cu and Fe K-edge X-ray absorption spectroscopy (XAS) measurements, at ca. 7112 and 8979 eV, respectively, are conducted at the Quick X-ray Absorption and Scattering (QAS) beamline (7-BM) of the National Synchrotron Light Source II (NSLS II) at Brookhaven National Laboratory (BNL). Fe-K_β X-ray emission spectroscopy (XES) data are obtained at the PIPOXS (2A) station at the Cornell High Energy Synchrotron Source (CHESS). The emission spectra are collected at room temperature from 7027 eV to 7089 eV with a step size of 0.41 eV for Fe samples. X-ray diffraction (XRD) data are collected on a Bruker D8 X-ray diffractometer equipped with a GADDS area detector (Cu $K\alpha$ radiation, ∼1.54 Å). Inductive plasma coupling spectroscopy-mass spectroscopy (ICP-MS) samples are prepared by dissolving the nanocrystals in 2% nitric acid at a concentration between 1 and 1000 μg/L. The characterization is conducted by the Cornell University/Cornell Nutrient Analysis Laboratory using Spectro MS Spectro Analytical Instruments, Inc. Transmission electron microscopy (TEM) analysis is performed on an FEI Tecnai T12 transmission electron microscope operating at 120 kV with a LaB_6 tip. UV−vis spectroscopy measurements are performed on a Cary 5000 UV−vis−NIR (Aligent Technologies) (300−1500 nm, standard tungsten quartz and deuterium light source) and Ocean Optics UV−vis DH2000 BAL (300−900 nm, halogen and deuterium light source). Detailed experimental methods can be found in the Supporting Information (SI).

■ RESULTS AND DISCUSSION

Structural characterization of the $CuFeS_2$ nanocrystals using X-ray diffraction reveals that the initial Cu-rich mixed phases transition to pure chalcopyrite with increasing synthesis time and temperature. To study the structural evolution for $CuFeS_2$ nanocrystals during synthesis, two sets of experiments are

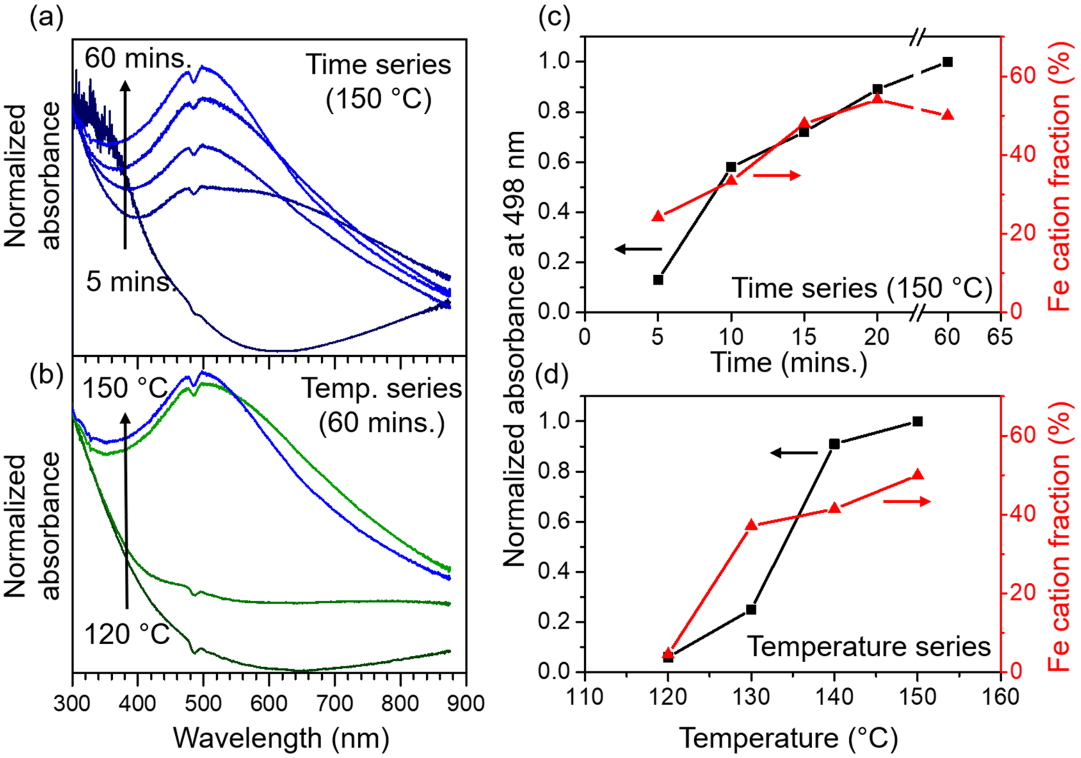

Figure 2. Plasmonic behavior of the $CuFeS_2$ time series and temperature series. (a) $CuFeS_2$ nanocrystals synthesized at 150 °C show a plasmonic peak for times ≥ 10 min and a gradual increase in the peak intensity with increasing synthesis time. (b) The temperature series shows a plasmon peak for nanocrystals synthesized at temperatures ≥ 130 °C, with a gradual increase in peak intensity. (c, d) Plot of absorbance at 498 nm (left y-axis) and cation fraction of Fe ($= \frac{M_{Fe}}{M_{Fe} + M_{Fe}} \times 100$)% measured by ICP-MS (right y-axis) for the (c) time series and (d) temperature series. The absorbance at 498 nm and Fe content gradually increase as reaction time and temperature increase. Note: The kink at 485 nm in all optical spectra is due to a detector artifact.

conducted: a temperature series and a time series. For the temperature series, the samples are soaked at four different temperatures (120, 130, 140, and 150 °C) for 60 min, and for the time series, the samples are soaked at 150 °C for different times ranging from 5 to 60 min. Details of the synthesis method can be found in the Supporting Information.

For the time series sample, the 5 min sample shows an asymmetric 47° XRD peak and broad peaks between 30° and 40°, indicating mixed phases (Figure 1a, top). On the basis of linear Gaussian fitting of the 47° peak with nonstoichiometric $CuFe_xS_y$ and $Cu_{2-x}S$ standards (Figures S2 and S4a), the 5 min sample is found to contain 87.5% bornite (Cu_5FeS_4, PDF #01-071-0368) and 12.5% chalcopyrite ($CuFeS_2$, PDF #01-070-8495) phases. With increasing reaction time (Figure 1a, top), the impurity peaks disappear and the intense XRD peak at 47° gradually shifts toward higher 2θ, aligning with the chalcopyrite phase peaks at 49.0° after 60 min, indicating the transitioning from a mixed phase to a single phase. This transitioning to a single phase is further evidenced by the symmetric 47° peak profile for time > 5 min samples. The anomalous peak intensity ratio between the 29.4° ((112) plane) and 49.0° peaks ((024) plane), compared to the standard pattern, is attributed to the flat disk morphology of the nanocrystals. The same XRD peak intensity inversion has been reported in other $CuFeS_2$ nanodisk studies.[23,32−34]

For the temperature series (Figure 1a, bottom), at the lowest temperature (120 °C), a mixed phase of djurleite and chalcopyrite is observed, as indicated by the 37.7° characteristic djurleite peak and the shoulder on the 47° peak in the diffraction pattern. Gaussian fitting (Figure S4b) shows the 120 °C sample to be a mix of 67.0% djurleite and 33.0% chalcopyrite. The remaining temperature series samples are single-phase based on the symmetric peak profile and the absence of impurity peaks. For samples with higher reaction temperatures, the 37.7° peak disappears and the initial peaks (120 °C) at 29.3°, 47°, and 57.8° shift toward higher 2θ; all of these peaks eventually align with the chalcopyrite standard, indicating the complete transition from djurleite to chalcopyrite. To be noted, the XRD pattern of 130 and 140 °C are almost identical, but they are both different from 150 °C, indicating that complete transformation occurs at or above 150 °C.

The cation ratios determined using inductively coupled plasma-mass spectroscopy confirms the transition from the djurleite to the chalcopyrite phase for both the time and temperature series samples. ICP-MS analysis (Figure S3) shows Cu-rich phases are initially present for both the time and temperature series samples (Fe to Cu ratio of 1:3 and 1:20, for 5 min−150 °C and 60 min−120 °C, respectively). The Fe to Cu molar ratio eventually converges to 1:1 for the 150 °C−60 min sample, confirming the formation of phase-pure chalcopyrite. Figure 1b shows the TEM image for the 140 °C $CuFeS_2$ nanocrystal as an example (see Figure S1 for full set of TEM data). TEM data show that, for the time series samples, the nanocrystal size gradually increases from 5.7 to 8.3 nm with a size dispersity of ∼11%, and for the temperature series samples, the size gradually increases from 4.4 to 8.3 nm with a dispersity of ∼10% (Figure 1c). Grain sizes determined

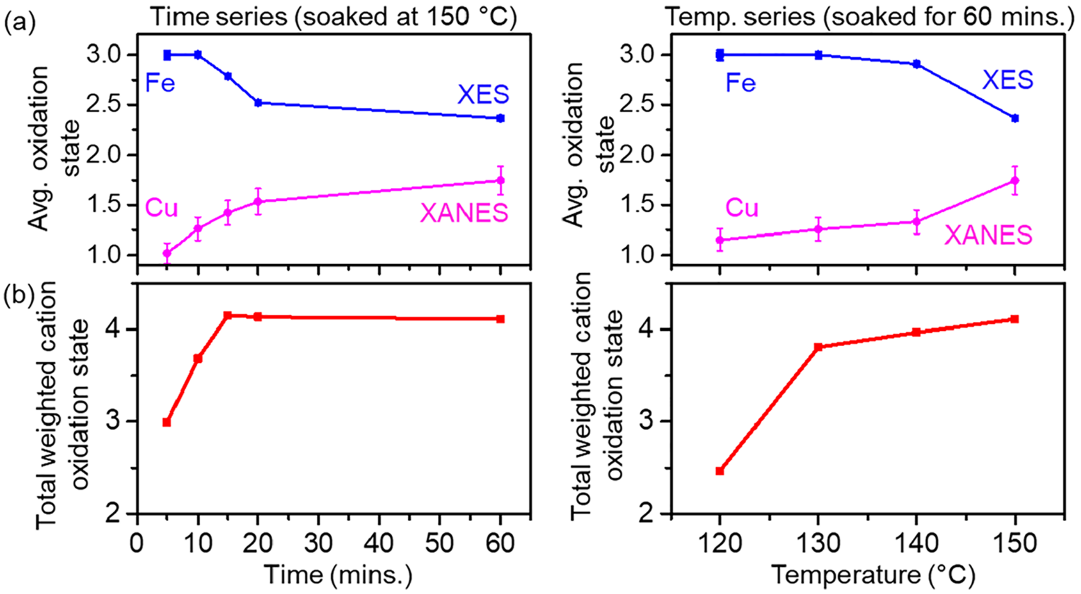

Figure 3. Oxidation state of cations. (a) Average oxidation state of Fe and Cu for time series (left) and temperature series (right). The Cu oxidation state of the samples is determined from X-ray absorption near-edge spectra (XANES) based on linear extrapolation of oxidation states vs edge energy plots of bulk standards (see SI). The Fe oxidation state of samples is determined using the more accurate method by collecting the Fe-edge $K_{\beta\text{-}1,3}$ (3p →1s) emission spectra (XES). The error bars are calculated based on the least-squares minimization fitting of the XES spectra. In both time and temperature series, the Cu oxidation state increases from 1+ to 1.75+ and the Fe oxidation state decreases from 3+ to 2.35+. (b) Total oxidation state of all cations in $Cu_xFe_yS_2$ are calculated by scaling oxidation state with cation fraction determined using ICP-MS (SI, eq S1). In both time (left) and temperature (right) series, the total cation oxidation state increases to 4+.

from Scherrer analysis using the XRD peaks are consistently smaller compared to the TEM sizes, indicating that our samples are multi-grained (Table S2).

The rich phase diagrams of both the Cu-Fe-S and Cu-S material systems span a variety of nonstoichiometric phases with similar XRD patterns (standards of all possible crystal structures in Figure S2). Therefore, it is essential to establish a method to identify the phase purity for the $CuFeS_2$ chalcopyrite phase using complementary characterization techniques. From our studies, we suggest a combination of XRD and elemental ratios (using ICP) to determine the phase purity. Phase-pure samples should show the four main chalcopyrite characteristic XRD peaks at approximately 29.4°, 33.8°, 49.0°, and 57.8°, and the pattern should not contain any impurity peaks. In addition, ICP results should indicate a 1:1 Fe to Cu cation ratio (±5% offset range due to ICP standard deviation). On the basis of these criteria, we identify the following samples to be phase-pure: (1) 15 min−150 °C, (2) 20 min−150 °C, and (3) 60 min−150 °C (Figure S3 and Table S3). Although these samples are best fitted by the chalcopyrite ($CuFeS_2$) phase, both the 15 and 20 min samples have an XRD peak at 48° that is shifted compared to the 49° from the chalcopyrite standard. This shift is attributed to the different Cu^{1+}/Cu^{2+} and Fe^{2+}/Fe^{3+} ratios in the samples. The sum of averaged oxidation states of a cation is observed to increase with reaction time (discussed in detail later), leading to stronger ionic bonds and smaller lattice spacing; hence, the XRD peaks are shifted to higher 2θ. This variability in oxidation states can explain the previously reported disparities in cation oxidation state and plasmonic behavior. Applying this criteria to previous studies on $CuFeS_2$, we determine that Gurin *et al.*[35] were actually reporting an impurity phase due to the extra XRD peaks at 20° and 33°. Although not many compositional analyses exist, Pron *et al.*[11] reported an Fe-deficient sample that matches the chalcopyrite standard which should be considered as an Fe-deficient impure phase. Both examples illustrate a combination of XRD and elemental ratio analysis is required to determine the chalcopyrite phase purity.

Our $Cu_xFe_yS_2$ nanocrystals show an evolving plasmonic behavior with increasing reaction time and temperature, which is found to be correlated with cation concentration as well as phase evolution. In the 300−800 nm wavelength range, no plasmon is observed at short times (5 min) for the time series; then, at 10 min, a broad plasmon peak centered around 498 nm appears which sharpens and increases in intensity until the final sample at 60 min (Figure 2a). The plasmon peak position remains at around 498 nm throughout the experiment, consistent with the plasmon peak position previously reported for $CuFeS_2$.[12,20,23] For the temperature series, the plasmon appears at 130 °C as a very broad and low intensity band, then abruptly increases in intensity until the final 150 °C sample, which displays a strong plasmon peak (Figure 2b).

In the early stage of both time and temperature series (120 °C−60 min and 150 °C−5 min), a rise of the absorption edge is observed between 600 and 900 nm, which suggests a plasmon in the near-IR wavelength range. This band corresponds to plasmon peaks for impurity phases identified in XRD (Cu_5FeS_4 and $Cu_{1.94}S$).[3,11] As the phase transforms to pure $CuFeS_2$, the characteristic plasmon at 498 nm is observed. Moreover, in both sample sets, a correlation is observed between the plasmon peak intensity and the Fe cation fraction $\left(=\left(\frac{M_{Fe}}{M_{Fe}+M_{Cu}}\times 100\right)\%\right.$, where M_{Fe} and M_{Cu} are the molar concentrations of Fe and Cu, respectively). For the time series samples, as the plasmon peak intensity gradually increases with reaction time, the Fe content increases from 24% to 50% (Figure 2c and Figure S3), accompanied by a phase transformation from a djurleite ($Cu_{1.94}S$) and chalcopyrite ($CuFeS_2$) mixed phase to a pure chalcopyrite ($CuFeS_2$) phase. For the temperature series, as the plasmon intensity increases

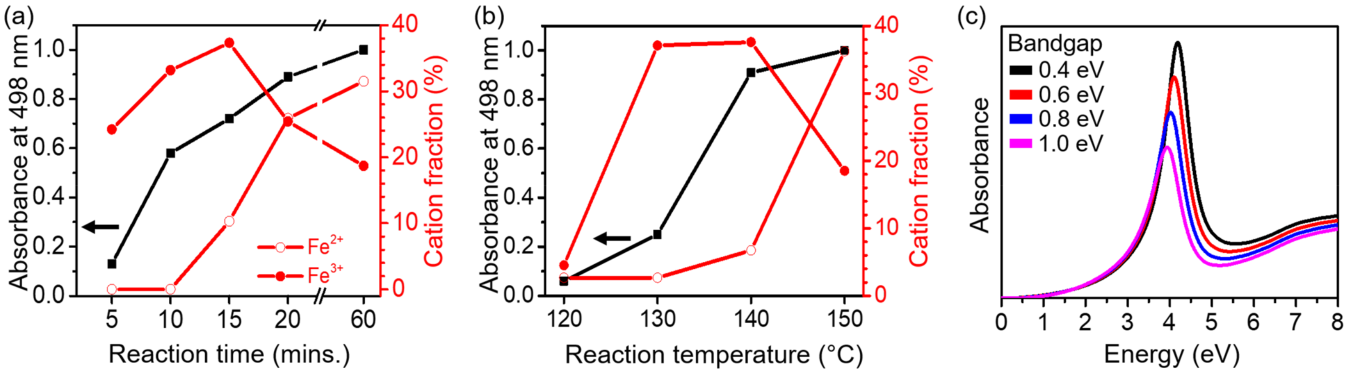

Figure 4. Correlation between Fe^{2+} and Fe^{3+} fraction (of all cations) (of) and plasmon peak intensity. Normalized absorbance at 498 nm (left *y*-axis, black) plotted against Fe^{2+} and Fe^{3+} fraction over all cations(calculated from ICP and *ex-situ* XES data, right *y*-axis, red) for (a) time series samples and (b) temperature series samples. A positive correlation is observed between the Fe^{2+} cation fraction and the plasmon peak intensity. (c) Simulated absorption spectrum with different band gap (BG) values for the valence to intermediate band gap (0.4 to 1.0 eV) using the linear optical model.

with temperature, the Fe content dramatically increases from 4% at 120 °C and 37% at 130 °C to 41% at 140 °C, then levels off to 50% at 150 °C (Figure 2d and Figure S3). This indicates that the Fe content has a positive correlation with the plasmon intensity.

Interestingly, the 130 °C and 140 °C temperature series samples have almost identical XRD patterns and similar Fe cation fraction but distinctive plasmonic behavior. The divergence between samples with identical long-range structural order and similar Fe content, but different optical behavior, indicates factors such as cation oxidation state could be affecting the electronic structure which leads to different plasmonic behaviors.

Through XANES and XES, we find that Fe incorporation in the nanocrystals with increasing reaction time and temperature is accompanied by a redox reaction between the Fe and Cu cations (raw data in Figures S6 and S7). XANES was used to characterize both cations. Due to low Fe content in the low-temperature and low-reaction-time samples, the XANES spectra showed poor signal intensity and concomitantly high error when analyzed for the oxidation states (Figure S6). Therefore, for more accurate determination of the oxidation states of the Fe ions, redundant characterization was performed using the K_β XES technique.[36,37] The average oxidation state of Fe cations determined using XANES and XES shows only a minor deviation from each other (Figure S9); however, significantly lower error values are observed in XES analysis (Figure S9, inset). In both synthesis pathways, the oxidation state of Fe decreases from 3+ to 2.35+ (Figure 3a). For the final samples (60 min−150 °C), the presence of both Fe^{2+} and Fe^{3+} and an average oxidation state of 2.35+ indicates only a partial reduction of the Fe^{3+} species to Fe^{2+}. For Cu, both synthesis pathways lead to an oxidation state increase from 1+ to 1.75+ (Figure 3a). Although a Cu^{2+} precursor is used for the synthesis of the nanocrystals, Cu^{1+} species are identified as the initial oxidation state during all synthesis pathways, likely due to reduction of Cu by oleylamine during the preparation of the metal precursor. On the basis of these trends in the cation chemistry, we conclude that Fe incorporation into the nanocrystals is accompanied by a redox reaction between the Fe and Cu cations, due to which the Fe^{3+}/Cu^{1+} partially changes to Fe^{2+}/Cu^{2+}. To confirm mixed cation oxidation states in CuFeS$_2$, we synthesized CuFeS$_2$ using Fe^{2+} precursor instead of Fe^{3+} precursor. A similar CuFeS$_2$ formation process, crystal structure transformation, and plasmon switching is observed, as confirmed by XRD and UV−vis spectrum (Figure S12), adding another degree of confidence for the proposed mixed Cu^{2+}/Cu^{1+} and Fe^{2+}/Fe^{3+} oxidation states.

The total weighted oxidation state of all cations, calculated by multiplying the oxidation state (XES, XANES) by the species' cation fraction (ICP-MS) (calculation details in SI, eq S1), increases from 3+ for the time series and 2.5+ for the temperature series to 4+ with increasing reaction time and temperature (Figure 3b). The initial lower value for total weighted oxidation state is attributed, again, to the initial formation of copper sulfide (djurleite, $Cu_{1.94}S$, with Cu^{1+}). As the phase transforms to the chalcopyrite phase, Fe cations are incorporated into the lattice, due to which an ideal total oxidation state of 4+ value is observed. This increase in the total oxidation state with time and temperature corroborates the observed shifts in the XRD peak positions: with increased total oxidation state, stronger ionic bonds are expected, which leads to a shorter average bond length and hence a shift of the XRD peaks to higher 2θ. Moreover, the changes in oxidation state have a major effect on the plasmonic behavior. For instance, the 130 and 140 °C samples show identical XRD patterns and have nearly the same Fe content (see Figures 1 and 2); however, their plasmon peak intensity greatly differs. The extracted cation oxidation states of the 130 and 140 °C samples show the average Cu oxidation state increases from 1.27+ to 1.33+ and average Fe oxidation state decreases from 2.98+ to 2.90+. The distinctive change in plasmonic behavior with minute changes in the cation's oxidation state indicates that the cation oxidation state (i.e., the electronic structure) plays a critical role in plasmon formation.

The cation fractionof Fe^{2+}

$$\left(= \frac{M_{Fe^{2+}}}{M_{Fe^{3+}} + M_{Fe^{2+}} + M_{Cu^{1+}} + M_{Cu^{2+}}} \times 100\right)\%$$

(determined using ICP and *ex situ* XES) is found to be positively correlated to the absorbance peak intensity (Figure 4). For the reaction time series, the Fe^{2+} cation fraction increases from 0% to 32% over the full series as the plasmon absorption increases (Figure 4a). The Fe^{3+} content, however, initially increases from 24% to 33% as the reaction time increases, and then decreases to 18%. For the temperature series, the Fe^{2+} cation concentration increases monotonically from 0% to 37% as the temperature increases (Figure 4b). The

Fe^{3+} concentration shows a similar trend as the time series; it initially increases from 4.5% to 33% and then drops to 18% for the final sample.

The relationship between the Fe^{2+} content and the plasmon intensity can be explained by the changes to the band gap between the valence band and intermediate band. From the data presented, there is clearly a direct correlation between the Fe^{2+} content and the plasmon intensity, indicating that the Fe^{2+}/Fe^{3+} ratio can determine the existence of a plasmon feature. The Fe^{2+}/Fe^{3+} ratio also has a directly observable effect on the band structure: in the 150 °C time series, as the reaction time increases, the Fe^{2+} cation concentration increases and the optical band gap decreases, from 1.71 eV (15 min) to 1.65 eV (20 min), and to 1.59 eV (60 min) (Figure S5). A similar correlation between band gap reduction with increased synthesis time for $CuFeS_2$ has been previously reported.[20] This change in band gap with Fe^{2+} content has also been reported in related systems: several experimental and theoretical studies have noted that Fe^{2+} incorporation leads to the shrinkage of the band gap.[38−40] For instance, DFT studies[40] of Fe_3O_4, which contains both Fe^{2+} and Fe^{3+}, reveal that, compared to Fe^{3+}, Fe^{2+} corresponds to a state with an additional electron in the lowest unoccupied t_{2g} orbital. For $CuFeS_2$, the calculated density of states indicates the intermediate band is mainly contributed by Fe 3d orbitals.[23] Therefore, having more Fe^{2+} in the $CuFeS_2$ system effectively lowers the intermediate band edge and leads to a narrower valence to intermediate band gap.

The decreased band gap leads to an increased plasmon feature due to the unique band structure of $CuFeS_2$. The plasmon in $CuFeS_2$ is produced by collective electronic transitions between the valence band and the intermediate band, as described by a linear optical model with Lorentz-like contributions to the permittivity.[41] Shrinking of the band gap leads to more electronic transitions between the valence band and intermediate band, which facilitates the formation of a more prominent plasmon. To qualitatively model the correlation between the band gap size and the plasmon formation, we adopt the simple linear optical model from Manna *et al.*[41] (see SI). Due to the dominant role of the Fe 3d orbital in the intermediate band, we extend the intermediate band closer to the valence band to simulate the effect of band narrowing. As shown in Figure 4c, a narrower valence to intermediate band gap leads to the formation of a stronger plasmon peak which matches our experimental observations. In summary, the increased Fe^{2+} content leads to lowering of the intermediate band which causes a more prominent plasmon peak.

To examine the temporal progression of the cation oxidation states and their relation to temperature, we conducted *in situ* Cu and Fe K-edge XAS experiments (Figure 5, raw data in Figure S8). In both experiments, the XAS data collection starts at 50 °C during the heating stage, and time = 0 min corresponds to the time when the target reaction temperature is reached. The reaction is continued for 30 min at the target reaction temperatures before cooling down. To be noted, in these *in situ* XAS experiments, the measured cation oxidation state is an average of ions in solution and ions in the nanocrystals. During the heat-up stage, the oxidation state of Cu remains relatively constant. However, after reaching the target reaction temperature, the redox behavior diverts between the two temperature conditions (Figure 5a). At 120 °C, the oxidation state of Cu remains unchanged at 1+, whereas a sharp increase in Cu oxidation state from 1+ to 1.6+ is observed at 150 °C. Interestingly, thereafter, during the reaction stage at 150 °C, the Cu oxidation state remains relatively constant. As for Fe, during the heat-up period, the Fe oxidation state slightly decreases from 3+ to 2.95+ at both temperatures (Figure 5b). This small change in Fe oxidation state is due to the partial reduction of Fe by the oleylamine at elevated temperatures. During the reaction stage, the oxidation state of Fe remains unchanged at 120 °C. However, at 150 °C, the oxidation state of Fe monotonically decreases to 2.6+ after 35 min, indicating a partial transition from Fe^{3+} to Fe^{2+}. Overall, the rapid increase of Cu oxidation state versus gradual change of Fe at 150 °C agrees well with our *ex situ* XAS and XRD results. The sudden Cu oxidation state change at time = 0 min is due to the initial rapid formation of the Cu-rich chalcopyrite phase, followed by gradual incorporation of Fe into the lattice. To confirm the optical behavior consistency between our *in situ* XAS experiments and our *ex situ* experiments, we replicated the *in situ* heat-up experiment environment in a laboratory setup and extracted the solution after reaching the required temperature and time (Figure S11). As expected, a plasmon is observed for the 150 °C sample and no plasmon for the 120 °C sample.

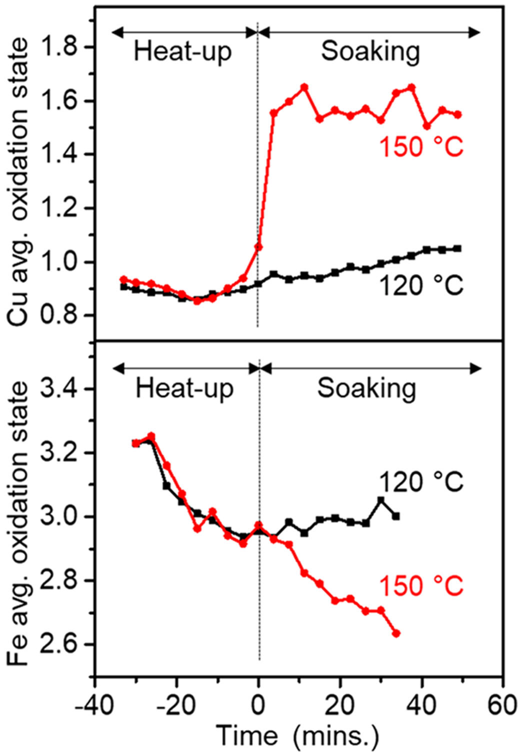

Figure 5. XANES analysis of *in situ* Cu and Fe K-edge XAS experiment at 120 and 150 °C. The data collection starts from 50 °C; 0 min is defined as the point at which the target reaction temperature has been reached. (a) Average oxidation state of Cu during *in situ* XAS experiment at 120 and 150 °C. (b) Average oxidation state of Fe during *in situ* XAS experiment at 120 and 150 °C.

On the basis of the *in situ* and *ex situ* XAS experiment, we propose a two-stage chemical reaction to explain the formation of $CuFeS_2$.

$$(2-x)Cu^{1+} + S^{2-} \rightarrow Cu_{2-x}S \tag{1}$$

$$\mathrm{Cu}_{2-x}^{1+}\mathrm{S} + (2-x)\mathrm{Fe}^{3+} + (3-2x)\mathrm{S}^{2-} \rightarrow (2-x)\mathrm{Cu}^{1+/2+}\mathrm{Fe}^{2+/3+}\mathrm{S}_2 \qquad (2)$$

In stage one (heat-up phase, i.e., time < 0 min), Cu ions react with sulfur to form $Cu_{2-x}S$ seeds. In stage two (soaking phase, i.e., time ≥ 0 min), Fe steadily incorporates into the $Cu_{2-x}S$, accompanied by a phase transition to the chalcopyrite phase. The initial $Cu_{2-x}S$ formation is due to the high reactivity between Cu and S at low temperature, which has been previously evidenced through the nucleation of $Cu_{2-x}S$ seeds at 50 °C.[42] The Fe-deficient chalcopyrite phase particle that is observed in the *ex situ* time study indicates a rapid phase transformation from the $Cu_{2-x}S$ phase to the chalcopyrite phase as Fe incorporates into the $Cu_{2-x}S$ seeds, which is accompanied by a partial Fe^{3+} to Fe^{2+} transition. The phase transformation could be induced by an Fe ion substitution with a Cu cation or incorporation into a $Cu_{2-x}S$ vacancy.

Both the *in situ* and *ex situ* XAS experiments show that the end product, $CuFeS_2$, has a mixed cation oxidation state of Cu^{2+}/Cu^{1+} and Fe^{2+}/Fe^{3+}. We attribute the conflicting results in previous experimental and theoretical reports to the ability of the chalcopyrite lattice structure to support a variable range of cation oxidation states. This finding is consistent with previous research in spinel oxides which have shown that different reaction temperatures can lead to different cation oxidation states for nanocrystals with the same structure and cation stoichiometry.[37,43]

CONCLUSION

In conclusion, we investigate the origin of plasmonic behavior in $CuFeS_2$ nanocrystals. We propose that the chalcopyrite phase ($CuFeS_2$) has a non-fixed cation oxidation state, and the ratio between Cu^{2+}/Cu^{1+} and Fe^{2+}/Fe^{3+} is determined by the synthesis conditions. Due to the existence of numerous nonstoichiometric phases in the Cu-Fe-S material system, a combination of XRD and ICP is required to identify the phase purity. As criteria for "phase purity", we suggest that samples have major XRD peaks at 29.4°, 33.8°, 49.0°, and 57.8°. In addition, the Cu to Fe ratio should be 1:1 with a 5% variation from this value. Since different $CuFeS_2$ nanocrystals can have the same phase but show distinctively different plasmonic behavior, we conclude that the plasmon is determined by the cation ratio and oxidation state but not the long-range order. *Ex situ* and *in situ* XAS/XES studies along with optical modeling identify that the incorporation of Fe^{2+} in the nanocrystal leads to shrinkage of the valence band to intermediate band band gap which causes plasmon formation. Moreover, our XAS and XRD data also unveil the reaction mechanism for the $CuFeS_2$ synthesis is composed of a two-step reaction: (1) initial formation of djurleite $Cu_{2-x}S$ seeds and (2) rapid Cu-rich chalcopyrite phase formation with gradual Fe incorporation which eventually transforms to pure chalcopyrite phase. The final $CuFeS_2$ shows a mixture of Cu^{2+}/Cu^{1+} and Fe^{2+}/Fe^{3+}. Overall, our work for $CuFeS_2$ serves as a model for studying intermediate band ternary plasmonic NCs.

ASSOCIATED CONTENT

Supporting Information

The Supporting Information is available free of charge at https://pubs.acs.org/doi/10.1021/acs.chemmater.0c03829.

Experimental details, Scherrer analysis, linear optical Lorentzian modeling, structural characterization using TEM, XRD, ICP, UV−vis, XAS, and XES (PDF)

AUTHOR INFORMATION

Corresponding Author

Richard D. Robinson − *Department of Materials Science and Engineering, Cornell University, Ithaca, New York 14853, United States;* orcid.org/0000-0002-0385-2925; Email: rdr82@cornell.edu

Authors

Yuan Yao − *Department of Materials Science and Engineering, Cornell University, Ithaca, New York 14853, United States;* orcid.org/0000-0002-4784-2753

Anuj Bhargava − *Department of Materials Science and Engineering, Cornell University, Ithaca, New York 14853, United States;* orcid.org/0000-0002-5961-6171

Complete contact information is available at: https://pubs.acs.org/10.1021/acs.chemmater.0c03829

Author Contributions

[†]These authors contributed equally.

Notes

The authors declare no competing financial interest.

ACKNOWLEDGMENTS

This work was supported in part by the National Science Foundation (NSF) under award numbers DMR-2003431, CHE-1665305, and CHE-1507753. The XES experiments made use of the Cornell Centre for Materials Research (CCMR), and Cornell High Energy X-ray Sciences (CHEXS) facilities funded in part by the National Science Foundation under award numbers DMR-1719875 and DMR-1829070. The X-ray absorption spectroscopy experiments were performed using beamline 7-BM (QAS) of the National Synchrotron Light Source II, a U.S. DOE Office of Science User Facility operated for the DOE Office of Science by Brookhaven National Laboratory under Contract No. DE-SC0012704. We would like to thank Steven Ehrlich, Lu Ma, and Marinkovic Nebojsa for helping with the XAS experiment. Also, Kenneth D. Finkelstein and Christopher J. Pollock's help with the XES experiments is greatly appreciated. Finally, we would like to thank Tatyana Dokuchayeva from Cornell Nutrient Analysis Laboratories for helping us with the ICP.

REFERENCES

(1) Schimpf, A. M.; Thakkar, N.; Gunthardt, C. E.; Masiello, D. J.; Gamelin, D. R. Charge-tunable quantum plasmons in colloidal semiconductor nanocrystals. *ACS Nano* **2014**, *8* (1), 1065−1072.

(2) Kanehara, M.; Koike, H.; Yoshinaga, T.; Teranishi, T. Indium tin oxide nanoparticles with compositionally tunable surface plasmon resonance frequencies in the near-IR region. *J. Am. Chem. Soc.* **2009**, *131*, 17736−17737.

(3) Luther, J. M.; Jain, P. K.; Ewers, T.; Alivisatos, A. P. Localized surface plasmon resonances arising from free carriers in doped quantum dots. *Nat. Mater.* **2011**, *10*, 361−366.

(4) Zhao, Y.; Pan, H.; Lou, Y.; Qiu, X.; Zhu, J.; Burda, C. Plasmonic $Cu_{2-x}S$ nanocrystals: Optical and structural properties of copper-deficient copper(I) sulfides. *J. Am. Chem. Soc.* **2009**, *131*, 4253−4261.

(5) Zandi, O.; Agrawal, A.; Shearer, A. B.; Reimnitz, L. C.; Dahlman, C. J.; Staller, C. M.; Milliron, D. J. Impacts of surface depletion on the plasmonic properties of doped semiconductor nanocrystals. *Nat. Mater.* **2018**, *17* (8), 710−717.

(6) Agrawal, A.; Kriegel, I.; Runnerstrom, E. L.; Scotognella, F.; Llordes, A.; Milliron, D. J. Rationalizing the Impact of Surface Depletion on Electrochemical Modulation of Plasmon Resonance Absorption in Metal Oxide Nanocrystals. *ACS Photonics* **2018**, *5* (5), 2044–2050.

(7) Agrawal, A.; Johns, R. W.; Milliron, D. J. Control of Localized Surface Plasmon Resonances in Metal Oxide Nanocrystals. *Annu. Rev. Mater. Res.* **2017**, *47* (1), 1–31.

(8) Caldwell, A. H.; Ha, D.; Ding, X.; Robinson, R. D. Analytical Modeling of Localized Surface Plasmon Resonance in Heterostructure Copper Sulfide Nanocrystals. *J. Chem. Phys.* **2014**, *141*, 164125.

(9) Niezgoda, J. S.; Yap, E.; Keene, J. D.; McBride, J. R.; Rosenthal, S. J. Plasmonic $CuxIn_yS_2$ quantum dots make better photovoltaics than their nonplasmonic counterparts. *Nano Lett.* **2014**, *14* (6), 3262–3269.

(10) Zhao, W.; Liang, F.; Jin, Z.-M.; Shi, X.-B.; Yin, P.-H.; Wang, X.-R.; Sun, C.; Gao, Z.-Q.; Liao, L.-S. Efficient plasmonic photocatalytic activity on silver-nanoparticle- decorated $AgVO_3$ nanoribbons. *J. Mater. Chem. A* **2014**, *2* (33), 13226–13231.

(11) Gabka, G.; Bujak, P.; Ostrowski, A.; Tomaszewski, W.; Lisowski, W.; Sobczak, J. W.; Pron, A. Cu-Fe-S Nanocrystals Exhibiting Tunable Localized Surface Plasmon Resonance in the Visible to NIR Spectral Ranges. *Inorg. Chem.* **2016**, *55*, 6660–6669.

(12) Bhattacharyya, B.; Pandey, A. $CuFeS_2$ Quantum Dots and Highly Luminescent $CuFeS_2$ Based Core/Shell Structures: Synthesis, Tunability, and Photophysics. *J. Am. Chem. Soc.* **2016**, *138* (32), 10207–10213.

(13) Carpenter, F. B. Estimation of pyrrhotite in pyrites ore. *J. Am. Chem. Soc.* **1900**, *22* (10), 634–637.

(14) Donnay, G.; Corliss, L. M.; Donnay, J. D. H.; Elliott, N.; Hastings, J. M. Symmetry of magnetic structures: Magnetic structure of chalcopyrite. *Phys. Rev.* **1958**, *112* (6), 1917–1923.

(15) Teranishi, T. Magnetic and electric properties of chalcopyrite. *J. Phys. Soc. Jpn.* **1961**, *16*, 1881–1887.

(16) Teranishi, T.; Sato, K.; Kondo, K. Optical properties of a magnetic semiconductor: Chalcopyrite $CuFeS_2$. I. Absorption spectra of $CuFeS_2$ and Fe-doped $CuAlS_2$ and $CuGaS_2$. *J. Phys. Soc. Jpn.* **1974**, *36* (6), 1618–1624.

(17) Kambara, T. Optical properties of a magnetic semiconductor: Chalcopyrite CuFeS. II. Calculated electronic structures of $CuGaS_2$: Fe and $CuFeS_2$. *J. Phys. Soc. Jpn.* **1974**, *36* (6), 1625–1635.

(18) Sato, K.; Teranishi, T. Optical Absorption Spectrum of a Thin $CuFeS_2$ Film. *J. Phys. Soc. Jpn.* **1976**, *40* (1), 297–298.

(19) Oguchi, T.; Sato, K.; Teranishi, T. Optical Reflectivity Spectrum of a $CuFeS_2$ Single Crystal. *J. Phys. Soc. Jpn.* **1980**, *48* (1), 123–128.

(20) Sugathan, A.; Bhattacharyya, B.; Kishore, V. V. R.; Kumar, A.; Rajasekar, G. P.; Sarma, D. D.; Pandey, A. Why Does $CuFeS_2$ Resemble Gold? *J. Phys. Chem. Lett.* **2018**, *9* (4), 696–701.

(21) Tsujii, N.; Mori, T. High thermoelectric power factor in a carrier-doped magnetic semiconductor $CuFeS_2$. *Appl. Phys. Express* **2013**, *6* (4), 043001.

(22) Ding, W.; Wang, X.; Peng, H.; Hu, L. Electrochemical performance of the chalcopyrite $CuFeS_2$ as cathode for lithium ion battery. *Mater. Chem. Phys.* **2013**, *137* (3), 872–876.

(23) Ghosh, S.; Avellini, T.; Petrelli, A.; Kriegel, I.; Gaspari, R.; Almeida, G.; Bertoni, G.; Cavalli, A.; Scotognella, F.; Pellegrino, T.; Manna, L. Colloidal $CuFeS_2$ nanocrystals: Intermediate Fe d-band leads to high photothermal conversion efficiency. *Chem. Mater.* **2016**, *28* (13), 4848–4858.

(24) Bastola, E.; Bhandari, K. P.; Subedi, I.; Podraza, N. J.; Ellingson, R. J. Structural, optical, and hole transport properties of earth-abundant chalcopyrite ($CuFeS_2$) nanocrystals. *MRS Commun.* **2018**, *8* (3), 970–978.

(25) Kowalik, P.; Bujak, P.; Penkala, M.; Kotwica, K.; Kmita, A.; Gajewska, M.; Ostrowski, A.; Pron, A. Synthesis of $CuFeS_{2-x}Se_x$-alloyed nanocrystals with localized surface plasmon resonance in the visible spectral range. *J. Mater. Chem. C* **2019**, *7* (21), 6246–6250.

(26) Yan, T.; Li, Y.; Song, X.; Wang, J.; Xie, Z.; Deng, D. Highly luminescent NIR-emitting $CuFeS_2$/ZnS core/shell quantum dots for optical imaging of inflamed tissue. *J. Mater. Chem. C* **2019**, *7* (24), 7279–7287.

(27) Todd, E. C.; Sherman, D. M.; Purton, J. A. Surface oxidation of chalcopyrite ($CuFeS_2$) under ambient atmospheric and aqueous (pH 2–10) conditions: Cu, Fe L- and O K-edge X-ray spectroscopy. *Geochim. Cosmochim. Acta* **2003**, *67*, 2137–2146.

(28) Mikhlin, Y.; Tomashevich, Y.; Tauson, V.; Vyalikh, D.; Molodtsov, S.; Szargan, R. A comparative X-ray absorption near-edge structure study of bornite, Cu_5FeS_4, and chalcopyrite, $CuFeS_2$. *J. Electron Spectrosc. Relat. Phenom.* **2005**, *142*, 83–88.

(29) Hu, J.; Lu, Q.; Deng, B.; Tang, K.; Qian, Y.; Li, Y.; Zhou, G.; Liu, X. A hydrothermal reaction to synthesize $CuFeS_2$ nanorods. *Inorg. Chem. Commun.* **1999**, *2* (12), 569–571.

(30) Boekema, C.; Krupski, A. M.; Varasteh, M.; Parvin, K.; Van Til, F.; Van Der Woude, F.; Sawatzky, G. A. Cu and Fe valence states in $CuFeS_2$. *J. Magn. Magn. Mater.* **2004**, *272–276*, 559–561.

(31) Pearce, C. I.; Pattrick, R. A. D.; Vaughan, D. J.; Henderson, C. M. B.; van der Laan, G. Copper oxidation state in chalcopyrite: Mixed Cu d^9 and d^{10} characteristics. *Geochim. Cosmochim. Acta* **2006**, *70*, 4635–4642.

(32) Wu, Y.; Zhou, B.; Yang, C.; Liao, S.; Zhang, W. H.; Li, C. $CuFeS_2$ colloidal nanocrystals as an efficient electrocatalyst for dye sensitized solar cells. *Chem. Commun.* **2016**, *52* (77), 11488–11491.

(33) Wang, Y. H. A.; Bao, N.; Gupta, A. Shape-controlled synthesis of semiconducting $CuFeS_2$ nanocrystals. *Solid State Sci.* **2010**, *12* (3), 387–390.

(34) Lyubutin, I. S.; Lin, C. R.; Starchikov, S. S.; Siao, Y. J.; Shaikh, M. O.; Funtov, K. O.; Wang, S. C. Synthesis, structural and magnetic properties of self-organized single-crystalline nanobricks of chalcopyrite $CuFeS_2$. *Acta Mater.* **2013**, *61* (11), 3956–3962.

(35) Malyarevich, A. M.; Yumashev, K. V.; Posnov, N. N.; Mikhailov, V. P.; Gurin, V. S. Optical transient bleaching and induced absorption of surface-oxidized Cu-Fe-S nanoparticles. *Appl. Phys. B: Lasers Opt.* **2000**, *70* (1), 111–116.

(36) Bhargava, A.; Chen, C. Y.; Finkelstein, K. D.; Ward, M. J.; Robinson, R. D. X-ray emission spectroscopy: An effective route to extract site occupation of cations. *Phys. Chem. Chem. Phys.* **2018**, *20*, 28990–29000.

(37) Bhargava, A.; Chen, C. Y.; Dhaka, K.; Yao, Y.; Nelson, A.; Finkelstein, K. D.; Pollock, C. J.; Caspary Toroker, M.; Robinson, R. D. Mn Cations Control Electronic Transport in Spinel $Co_xMn_{3-x}O_4$ Nanoparticles. *Chem. Mater.* **2019**, *31* (11), 4228–4233.

(38) Gao, Y.; Hou, Q.; Liu, Q. First-principles study on the electronic structures and magneto-optical properties of $Fe^{2+}/^{3+}$ doped SnO_2. *Solid State Commun.* **2020**, *305*, 113764.

(39) Lohar, G. M.; Jadhav, S. T.; Takale, M. V.; Patil, R. A.; Ma, Y. R.; Rath, M. C.; Fulari, V. J. Photoelectrochemical cell studies of Fe^{2+} doped ZnSe nanorods using the potentiostatic mode of electrodeposition. *J. Colloid Interface Sci.* **2015**, *458*, 136–146.

(40) Noh, J.; Osman, O. I.; Aziz, S. G.; Winget, P.; Brédas, J. L. A density functional theory investigation of the electronic structure and spin moments of magnetite. *Sci. Technol. Adv. Mater.* **2014**, *15* (4), 044202.

(41) Gaspari, R.; Della Valle, G.; Ghosh, S.; Kriegel, I.; Scotognella, F.; Cavalli, A.; Manna, L. Quasi-Static Resonances in the Visible Spectrum from All-Dielectric Intermediate Band Semiconductor Nanocrystals. *Nano Lett.* **2017**, *17*, 7691–7695.

(42) Williamson, C. B.; Nevers, D. R.; Hanrath, T.; Robinson, R. D. Prodigious Effects of Concentration Intensification on Nanoparticle Synthesis: A High-Quality, Scalable Approach. *J. Am. Chem. Soc.* **2015**, *137*, 15843–15851.

(43) Dorris, S. E.; Mason, T. O. Electrical Properties and Cation Valencies in Mn_3O_4. *J. Am. Ceram. Soc.* **1988**, *71* (5), 379–385.